Atmospheric
Chemistry
and Physics
Discussions

1 **Measurement report: Diurnal variations of brown carbon during two distinct seasons in a**

2 **megacity in Northeast China**

3 Yuan Cheng[1], Xu-bing Cao[1], Jiu-meng Liu[1,*], Ying-jie Zhong[1], Qin-qin Yu[1], Qiang Zhang[2] and Ke-

4 bin He[3]

5 [1] State Key Laboratory of Urban Water Resource and Environment, School of Environment, Harbin

6 Institute of Technology, Harbin 150090, China

7 [2] Ministry of Education Key Laboratory for Earth System Modeling, Department of Earth System

8 Science, Tsinghua University, Beijing 100084, China

9 [3] State Key Joint Laboratory of Environment Simulation and Pollution Control, School of

10 Environment, Tsinghua University, Beijing 100084, China

11 *Corresponding author. Jiu-meng Liu (jiumengliu@hit.edu.cn).

12 **Abstract**

13 Brown carbon (BrC) represents an important target for the "win-win" strategy of mitigating climate

14 change and improving air quality. However, estimating co-benefits of BrC control remains difficult

15 for China, partially because current measurement results are insufficient to represent the highly

16 variable emission sources and meteorological conditions across different regions. In this study, we

17 investigated, for the first time, the diurnal variations of BrC during two distinct seasons in a largely

18 unexplored megacity in Northeast China. The winter campaign conducted in January of 2021 was

19 characterized by low temperatures rarely seen in other Chinese megacities (down to about –20 °C).

20 The mass absorption efficiencies of BrC at 365 nm (MAE_{365}) were found to be ~10% higher at night.

21 The variations of MAE_{365} could not be explained by the influence of residential biomass burning

22 emissions or secondary aerosol formation, but were strongly associated with the changes of a

23 diagnostic ratio for the relative importance of coal combustion and vehicle emissions ($R_{S/N}$). Given

24 that most coal combustion activities were uninterruptible, the higher nighttime MAE_{365} in winter

25 were attributed primarily to increased emissions from heavy-duty diesel trucks. The spring

Atmospheric
Chemistry
and Physics
Discussions

26 campaign conducted in April of 2021 was characterized by frequent occurrences of agricultural fires,

27 as supported by the intensive fire hotspots detected around Harbin and the more-than-doubled

28 levoglucosan to organic carbon ratios (LG/OC) compared to winter campaign. In spring, MAE_{365}

29 depended little on $R_{S/N}$ but exhibited a strong positive correlation with LG/OC, suggesting open

30 burning emissions as the dominant influencing factor for BrC's light absorption capacity. MAE_{365}

31 were ~70% higher at night for the spring campaign, pointing to the prevalence of nighttime

32 agricultural fires, which were presumably in response to local bans on open burning. It is noteworthy

33 that the agricultural fire emissions resulted in distinct peak at ~365 nm for the light absorption

34 spectra of BrC, and a candidate for the compounds at play was inferred to be $C_7H_7NO_4$. Due to the

35 presence of the ~365 nm peak, the absorption Ångström exponents could not be properly determined

36 for the agricultural fire-impacted samples. In addition, the ~365 nm peak became much less

37 significant during the day, likely due to photo-bleaching of the relevant chromophores.

1. Introduction

Light-absorbing organic carbon, i.e., brown carbon (BrC), exerts important yet poorly understood effects on climate and the environment (Brown et al., 2018; Zeng et al., 2020; Sand et al., 2021). As a mixture of numerous organic compounds from both primary emissions and secondary formation, BrC exhibits extreme complexity in spectroscopy, composition and evolution (Laskin et al., 2015; Brege et al., 2021; Washenfelder et al., 2022). Measurement techniques for BrC absorption mainly fell into two categories, including solvent extraction followed by light absorption spectrum measurement (Chen and Bond, 2010; Hecobian et al., 2010) and apportionment of total aerosol absorption to the contributions from black carbon and BrC (Yang et al., 2009; Lack et al., 2012). So far, consistency between BrC results from these two types of approaches has not been addressed, with variable relationships, either linear or non-linear, and unclear influencing factors (Kumar et al., 2018; Zeng et al., 2022). This inconsistency introduced substantial difficulties to the integration of BrC measurement results across studies and regions (Wang et al., 2022), which is essential for unfolding the links between BrC sources and optical properties. In addition, efforts were also made to explain BrC absorption on a molecular level. Several techniques were shown to be powerful, such as electrospray ionization Fourier transform ion cyclotron resonance mass spectrometry (ESI FT-ICR MS; Wozniak et al., 2008; Jiang et al., 2021; Zeng et al., 2021), high performance liquid chromatography coupled with high resolution mass spectrometry (HPLC/HRMS; Lin et al., 2018; Huang et al., 2022; Xu et al., 2022), and two-dimensional gas chromatography with time of flight mass spectrometer (GC×GC-ToF-MS; Huo et al., 2021). These techniques were more frequently applied to laboratory-generated primary or secondary BrC (e.g., Lin et al., 2015), which usually had less complex composition than ambient BrC and thus showed

Atmospheric
Chemistry
and Physics
Discussions

60 relatively high fraction of resolvable chromophores, e.g., up to ~85% for those emitted by biomass

61 burning (Huang et al., 2022).

62   The absorbing nature of BrC makes it a non-negligible contributor to positive radiative forcing

63 (Saleh, 2020), while the considerable contribution of organic aerosol to fine particulate matter

64 ($PM_{2.5}$) makes BrC an important source of air pollution (Wang et al., 2019). Consequently, BrC

65 represents a key species for the "win-win" strategy of mitigating climate change and improving air

66 quality. Given the highly variable emission sources and meteorological conditions across different

67 regions in China, field observational results on BrC are far from being enough to constrain air

68 quality and climate models, limiting the ability to evaluate the co-benefits of BrC control. In this

69 study, we focused on a largely unexplored city cluster, the Harbin-Changchun (HC) metropolitan

70 area in Northeast China. Compared to other regions with intensive studies of BrC as well as other

71 air pollutants (e.g., the North China Plain), HC was characterized by extremely cold winter and

72 strong impacts of biomass burning on top of other anthropogenic emissions (e.g., from coal

73 combustion). The first feature was related to the relatively high latitudes of HC. For example, as the

74 northernmost megacity in China, Harbin has an average temperature of about –20°C in January,

75 significantly lower than that of Beijing. The second feature was related to the massive agricultural

76 sector in HC. Until recently, open burning was still an irreplaceable approach for the disposal of

77 crop residues in this region, presumably because the amount of agricultural wastes were too huge

78 for the capacity of sustainable use. The agricultural fires frequently resulted in heavily-polluted

79 episodes with high $PM_{2.5}$ concentrations rarely encountered in other Chinese megacities (e.g.,

80 hourly-average of ~1000 μg/m^3 in Harbin; Li et al., 2019). These two features highlighted the

81 uniqueness of HC for haze studies in China.

82 This measurement report, for the first time, presented field observational results on the diurnal

83 variations of BrC during two distinct seasons, i.e., a frigid winter and an agricultural fire-impacted

84 spring, in the central city of HC. Drivers for the diurnal variations were discussed based on

85 indicators of various sources. Particularly, the agricultural fires were found to result in unique

86 absorption spectra of brown carbon. This study provided implications for parameterization of BrC

87 in climate models.

88 **2. Methods**

89 **2.1 Field sampling**

90 Daytime and nighttime $PM_{2.5}$ samples were collected on the campus of Harbin Institute of

91 Technology (HIT) during winter and spring of 2021. HIT was surrounded by residential and

92 commercial areas, without major industrial sources nearby, and thus represented a typical urban site.

93 The sampling was done by a mass flow controlled high-volume sampler (TE-6070BLX-2.5-HVS;

94 Tisch Environmental, Inc., OH, USA), which was operated at a flow rate of 1.13 m^3/min using pre-

95 baked quartz-fiber filters ($8'' \times 10''$, 2500 QAT-UP; Pall Corporation, NY, USA). Daytime and

96 nighttime samples were collected from 9:00 to 16:00 and from 21:00 to 5:00 of the next day,

97 respectively. The winter campaign covered the entire January of 2021, and the spring campaign was

98 conducted during 10–30 April, 2021.

99 **2.2 Laboratory analysis**

100 Two punches with diameters of 20 mm were taken from each sample, combined and then

101 extracted by deionized water. The water extract was analyzed using a Dionex ion chromatography

102 system (ICS-5000$^+$; Thermo Fisher Scientific Inc., MA, USA). Levoglucosan, an organic tracer for

103 biomass burning, was determined by the high-performance anion-exchange chromatography

104   coupled to pulsed amperometric detection (HPAEC-PAD) method (Engling et al., 2006; Yttri et al.,

105   2015). Inorganic ions such as nitrate, sulfate, chloride, ammonium and potassium were also

106   measured. Linear regression of the total cation concentration on that of total anion (both in $\mu eq/m^3$)

107   led to a slope of 1.14 ± 0.01 (intercept was set as zero; $r = 0.99$), indicating a neutralized feature of

108   the Harbin aerosols.

109   Two punches with diameters of 47 mm were taken from each sample and used to determine

110   carbon fractions. One punch was directly measured for organic carbon and elemental carbon, while

111   the other punch was immersed in methanol (HPLC grade; Fisher Scientific Company L.L.C., NJ,

112   USA) for an hour without stirring or sonication, dried in air for another hour, and then analyzed.

113   Both punches were measured by a Thermal/Optical Carbon Analyzer (DRI-2001; Atmoslytic Inc.,

114   CA, USA), which was operated with two commonly-used temperature protocols (i.e., IMPROVE-

115   A and NIOSH) and transmittance charring correction. The difference of total carbon (TC)

116   concentrations between the untreated and extracted punches ($TC_{untreated} - TC_{extracted}$) was used to

117   represent the amount of organic carbon that is soluble in methanol (MSOC), following the method

118   developed by Chen and Bond (2010) and refined by Cheng et al. (2016). Given that the TC

119   measurement was independent of the temperature protocol used, both $TC_{untreated}$ and $TC_{extracted}$ were

120   determined as the averages of total carbon results from IMPROVE-A and NIOSH. A benefit of this

121   approach was that the uncertainty of MSOC (σ) could be estimated for each sample based on the

122   parallel TC measurements by different protocols:

123      $$\sigma = \sqrt{\left(SD\ of\ TC_{untreated}\right)^2 + \left(SD\ of\ TC_{extracted}\right)^2} \Big/ \left(TC_{untreated} - TC_{extracted}\right)$$

124   where SD indicates standard deviation. In this study, σ averaged $3.3 \pm 2.9\%$ with a median of 2.4%.

125   In addition, organic compounds that are in-soluble in methanol, i.e., MIOC, was measured as the

126 organic carbon concentration of the extracted punch. Unless stated otherwise, (i) OC involved in

127 the following discussions indicates the sum of MSOC and MIOC, and correspondingly, EC indicates

128 elemental carbon measured by the extracted punch; and (ii) all the carbonaceous aerosol

129 concentrations are based on IMPROVE-A, except MSOC which did not rely on analytical protocol.

130 The MSOC to OC ratios averaged 0.90 ± 0.05, indicating an overall high extraction efficiency of

131 methanol for dissolving organic aerosols.

132   Light absorption spectra of the methanol extracts were measured over the wavelength (λ) range

133 of 200–1110 nm, using a spectrophotometer coupled with a 2.5-m long liquid waveguide capillary

134 cell (LWCC; World Precision Instrument, FL, USA). The spectrophotometer, consisting of a DH-

135 mini UV-VIS-NIR light source and a Maya2000 Pro spectrometer (Ocean Optics Inc., FL, USA),

136 provided wavelength-resolved optical attenuation (ATN_λ) of the dissolved BrC, which could then

137 be converted to BrC absorption coefficient [$(b_{abs})_\lambda$] (Hecobian et al., 2010). The ratio of $(b_{abs})_\lambda$ to

138 MSOC concentration was considered the bulk mass absorption efficiency (MAE_λ) of brown carbon,

139 given the close-to-one MSOC/OC. The wavelength dependence of BrC absorption was determined

140 based on $\ln(ATN_\lambda)$ and $\ln(\lambda)$, and was expressed as the absorption Ångström exponent (AAE). The

141 AAE calculation was performed over 310–460 nm, the same λ range adopted by previous studies

142 conducted at the same site using the same laboratory analysis procedures (Cheng et al., 2022a).

143 **2.3 Additional data sets used**

144   Air quality data and meteorological data were obtained with a time resolution of 1 hour from

145 the China National Environmental Monitoring Center (CNEMC; https://air.cnemc.cn:18007/, last

146 access: 1 January, 2023) and Weather Underground (https://www.wunderground.com/, last access:

147 1 January, 2023), respectively. CNEMC operated 12 monitoring sites in Harbin, with 3 of them

148   located within ~5 km from the HIT sampling site. The reconstructed $PM_{2.5}$ masses, which were

149   derived from observational results on aerosol compositions at HIT, were generally in line with the

150   fine particle concentrations directly measured at the nearby CNEMC sites. Here the reconstructed

151    $PM_{2.5}$ was calculated as the sum of organic matter (1.6 ×OC), elemental carbon and inorganic ions.

152   Comparison of the reconstructed and directly-measured $PM_{2.5}$ concentrations showed relative

153   standard deviations of 9–11% (in terms of median value) for the three CNEMC sites nearby,

154   demonstrating HIT as a representative urban site for Harbin. In this study, only the air quality data

155   from the nearest CNEMC site, i.e., Taping Hongwei Park, were further investigated together with

156   the aerosol components measured at HIT.

157   **3. Results and discussion**

158   **3.1 Why was the wintertime brown carbon more absorbing at night?**

159   The wavelength-resolved b_{abs} and MAE were primarily explored at 365 nm, and the

160   corresponding values were referred to as $(b_{abs})_{365}$ and MAE_{365}, respectively. $(b_{abs})_{365}$ and MSOC

161   correlated strongly for the winter campaign (Figure 1a), that the linear regression of $(b_{abs})_{365}$ against

162   MSOC led to an r value of 0.97 and a slope of 1.63 ±0.02 m^2/gC (with the intercept set as zero;

163   MAE_{365} averaged 1.55 ± 0.18 m^2/gC). However, the nighttime samples were found to exhibit

164   slightly higher MAE_{365} values than the daytime ones, with averages of 1.61 ±0.15 and 1.48 ±0.18

165   m^2/gC, respectively (Figure 1b). In this study, we did not perform source apportionment analysis

166   for brown carbon due to the relatively small number of samples collected. Instead, several indirect

167   indicators were introduced to interpret the diurnal variations of MAE_{365}.

168   The first indicator was the levoglucosan to OC ratio (LG/OC; on a basis of carbon mass, the

169   same hereinafter). In general, higher LG/OC values indicate a stronger contribution of biomass

170   burning (BB) emissions to OC. The BB activities in January could be attributed primarily to

171   household use of biofuels, e.g., for heating and cooking. This is because (i) few fire hotspot was

172   detected in Harbin and surrounding regions throughout the winter campaign (Figure 2a), and (ii) the

173   relationship between LG and water-soluble potassium (K^+), another commonly-used BB tracer, did

174   not show evidence for apparent influence of open burning (Figure 3a). As suggested by previous

175   studies conducted during heating season in Harbin (Cheng et al., 2022b), the LG to K^+ ratios were

176   relatively low and constant (~0.5) with the absence of agricultural fires, but became substantially

177   higher (typically above 1.0) during open burning episodes. This pattern was attributed to the

178   relatively low combustion efficiencies (CE) of agricultural fires, which favored the increase of LG

179   emissions but would not change K^+ emissions significantly (Gao et al., 2003). It should be noted

180   that in Cheng et al. (2022b), CE were not directly measured for different types of burning activities

181   and instead were investigated based on the ratios of BB organic carbon to BB elemental carbon (R_{BB},

182   derived from positive matrix factorization, i.e., PMF, analysis). Substantial increases of R_{BB} were

183   repeatedly observed during open burning episodes occurring in different seasons, e.g., winter or

184   spring depending on the regulatory policies. Thus the agricultural fires were inferred to have

185   relatively low CE levels (Cheng et al., 2022b), as BB source emission studies typically showed a

186   decreasing trend for the emission ratio of organic carbon to elemental carbon with increasing

187   combustion efficiency (Pokhrel et al., 2016; McClure et al., 2020). Actually, crops residues burned

188   on farmland were usually not intentionally dried and thus could have relatively high water contents.

189   This may partially explain the relatively low CE of agricultural fires. In the present study, LG

190   correlated strongly with K^+ for the entire January ($r = 0.96$, with a slope, i.e., $\Delta LG/\Delta K^+$, of 0.55 ±

191   0.02; Figure 3a) and the LG to K^+ ratios averaged 0.46 ± 0.11, pointing to the dominance of

192   residential burning in BB emissions. In addition, the residential burning activities were more

193   intensive at night, as can be seen from the elevated LG/OC compared to daytime results (1.10 ±

194   0.26% vs. 0.88 ±0.22%; Figure 1c). Comparison of the LG to EC ratios between the nighttime and

195   daytime samples (0.22 ±0.06 vs. 0.15 ±0.05) reached the same conclusion. Indeed, biomass burning

196   could emit a number of strong chromophores such as nitrogen-containing aromatic compounds

197   (Mohr et al., 2013; Lin et al., 2016, 2017; Xie et al., 2019; Salvador et al., 2021). However, for the

198   January samples, MAE_{365} did not show clear dependence on LG/OC or LG/EC ($r = 0.42$ and 0.12,

199   respectively; Figure 1e), suggesting that in addition to BB emissions, there must exist other factors

200   that were more responsible for the diurnal variations of wintertime MAE_{365}.

201   The second indicator was $R_{S/N}$, defined as the ratio of (n-sulfur dioxide + n-sulfate) to (n-

202   nitrogen dioxide + n-nitrate), where "n" indicates molar concentration. Given that sulfate and nitrate

203   are typically considered as secondary, $R_{S/N}$ could be roughly traced back to the emission ratios of

204   sulfur dioxide (SO_2) to nitrogen oxides (NO_x), i.e., $E_{S/N}$, from combustion of various types of fuels

205   (e.g., coal, gasoline, diesel and biomass). Previous studies suggested that $E_{S/N}$ differed substantially

206   between emissions from vehicles, coal combustion and biomass burning. In China, the fuel quality

207   standards have been greatly strengthened for on-road vehicles since early 2000s, e.g., the maximum

208   sulfur content allowed in diesel was reduced from 2000 ppm (required by the China I standard

209   implemented in 2002) to 10 ppm (required by the China V standard implemented in 2017). Thus,

210   recent studies on vehicular exhausts typically suggested that the SO_2 emission factors (EF-SO_2)

211   were about two orders of magnitude lower than those of NOx (EF-NOx; Zhang et al., 2015; Li et

212   al., 2019) and consequently, the corresponding $E_{S/N}$ should be approximately $\sim 10^{-2}$. EF-SO_2 were

213   also usually lower than EF-NOx for biomass burning (Zhang et al., 2000; McMeeking et al., 2009;

214 Liu et al., 2016; Wu et al., 2022), but their differences were not as large as those observed in vehicle

215 emissions, leading to $E_{S/N}$ values of ~10^{-1}. Unlike vehicles or biomass burning, coal combustion

216 usually resulted in higher EF-SO_2 compared to EF-NO_x (Zhang et al., 2000; Du et al., 2017; Li et

217 al., 2017), which could be translated to $E_{S/N}$ values of above one. On the other hand, primary species

218 could be transformed rapidly during atmospheric aging, e.g., a sharp loss of NO_x and a

219 corresponding burst in nitrate were observed shortly after emission when tracking plumes from

220 diesel trucks (Shen et al., 2021) and agricultural fires (Akagi et al., 2012; Liu et al., 2016). Thus it

221 should be acceptable to assume that for the pollutants emitted by a specific source, the $R_{S/N}$ of aged

222 plumes was generally comparable with the $E_{S/N}$ of fresh emissions.

223   The ambient $R_{S/N}$ averaged 0.6 ± 0.2 during the winter campaign, differing substantially from

224 the $E_{S/N}$ of coal combustion or vehicle emissions but in the same order of magnitude as the $E_{S/N}$ of

225 biomass burning. Actually, no evidence supported BB emissions as a major regulating factor for

226 $R_{S/N}$, e.g., as indicated by the insignificant correlations between $R_{S/N}$ and LG/EC ($r = 0.24$ and 0.01

227 for the daytime and nighttime samples, respectively). Then $R_{S/N}$ was expected to be more sensitive

228 to the changes of coal combustion and vehicle emissions, e.g., increase of coal combustion

229 emissions would effectively elevate $R_{S/N}$ whereas higher vehicle emissions favor the decrease of

230 $R_{S/N}$. During the winter campaign, lower $R_{S/N}$ were observed at night (Figure 1d), averaging $0.5 \pm$

231 0.1 compared to an average $R_{S/N}$ of 0.7 ± 0.2 for the daytime samples. In principle, this pattern could

232 be caused by decreased coal combustion emissions and/or increased vehicle emissions at night.

233 However, it seemed that the former did not play an important role, since many coal combustion

234 activities (e.g., those for heating supply, power generation and some industrial processes) were

235 uninterruptible, i.e., would not be stopped at night (Lian et al., 2020; Chu et al., 2021; Yuan et al.,

236 2021). Then the most likely cause for the lower nighttime $R_{S/N}$ was increased vehicle emissions.

237 According to the Road Traffic Regulations released by Harbin, heavy-duty diesel trucks (HDDT),

238 which are known to include high- or super-emitters (Dallmann et al., 2012), are allowed to run on

239 the roads in the main urban area only from 21:00 to 5:00 of the next day. This to a large extent

240 explains the inference on the increase of vehicle emissions during nighttime. MAE_{365} exhibited a

241 clear negative dependence on $R_{S/N}$ for all the winter samples (Figure 1f), suggesting vehicle

242 emissions, especially those from HDDT, as a dominant influencing factor for MAE_{365} (under the

243 precondition of relatively stable coal combustion emissions).

244   The last two indicators were associated with secondary aerosol formation, including the sulfur

245 oxidation ratio (SOR) and the nitrogen oxidation ratio (NOR) defined as n-sulfate/(n-sulfate + n-

246 SO_2) and n-nitrate/(n-nitrate + n-NO_2), respectively. The entire winter campaign experienced low

247 temperatures, which averaged -16 ± 5 and -21 ± 6 °C for the daytime and nighttime samples,

248 respectively. In general, the transformation of gaseous precursors to secondary inorganic ions was

249 inefficient in the frigid atmosphere, as indicated by the overall low levels of both SOR and NOR.

250 However, both indicators exhibited noticeable differences between daytime and nighttime samples.

251 The diurnal variation of SOR was found to be associated with the higher relative humidity (RH)

252 levels at night (Figure 4a). For the vast majority of winter samples, RH fell into the ranges of 60–

253 80 and 70–90% during daytime and nighttime, respectively. SOR were largely unchanged when RH

254 increased from 60–70% to 70–80% during the day, whereas for the common RH range shared by

255 the daytime and nighttime samples (i.e., 70–80%), SOR were slightly lower at night, likely due to

256 the drop of temperatures. In addition, a positive dependence of SOR on RH was evident for the

257 nighttime samples. Although SOR showed almost the same median values (~0.1) for the RH ranges

258   of 70–80 and 80–90% at night, relatively high SOR levels of above 0.2 were more frequently

259   observed in the latter case. Such high SOR were rarely seen during the day, indicating that RH

260   played a more important role than temperature in sulfate formation. The enhanced sulfate formation

261   at high RH was presumably through heterogeneous reactions (Su et al., 2020; Liu et al., 2021), since

262   the low temperatures encountered during the winter campaign did not rule out the presence of

263   aerosol water, e.g., liquid water was observed to remain super-cooled in clouds down to

264   temperatures of as low as –40 °C (Tabazadeh et al., 2002). Compared to SOR, different patterns of

265   diurnal variation were observed for NOR (Figure 4b). First, the difference between daytime and

266   nighttime NOR was more significant for the RH range of 70–80%, e.g., as indicated by the larger

267   decrease of median NOR at night (0.06, compared to a corresponding value of 0.02 for SOR).

268   Second, the nighttime NOR elevated substantially as RH increased from 70–80% to 80–90%, but

269   still with lower levels compared to the daytime results. Given that relatively low temperatures favor

270   the partitioning of semi-volatile nitrate into aerosol phase, the less efficient nitrate formation at night

271   could not be explained by the partitioning process and instead should be primarily attributed to

272   reduced photooxidation of NO_2 (Chen et al., 2020). Based on a synthesis of the diurnal variations

273   observed for SOR and NOR, the nighttime samples were characterized by enhanced heterogeneous

274   chemistry, which did not require sunlight as indicated by the RH-dependent increase of SOR under

275   dark conditions, and weakened photochemical reactions. The overall effect of these two factors on

276   secondary organic aerosol (SOA) formation was inconclusive and thus it remained difficult to

277   unfold the role of SOA in the diurnal variations of MAE_{365}. Actually, it appeared that MAE_{365} was

278   not strongly influenced by SOA during the winter campaign. For example, when RH increased from

279   70–80% to 80–90% at night, the MAE_{365} were nearly constant (e.g., with the same average value of

280   1.6 m^2/gC for the two RH ranges) despite the enhancement of heterogeneous chemistry.

281   **3.2 Why did the springtime MAE_{365} show more significant diurnal variations?**

282   Compared to the wintertime results, the average MAE_{365} was lower in spring (1.33 vs. 1.55

283   m^2/gC) but the corresponding standard deviation was much higher (0.62 vs. 0.18 m^2/gC), indicating

284   that the spring samples varied more significantly with respect to the absorption capacity of brown

285   carbon (Figure 5a). This feature could also be seen from the more pronounced diurnal variations of

286   MAE_{365} observed in spring (Figure 5b), e.g., the nighttime MAE_{365} were on average ~70% and 10%

287   larger than the daytime values during the spring and winter measurement periods, respectively. For

288   the winter campaign, the slightly elevated MAE_{365} at night had been primarily attributed to increased

289   vehicle emissions, as indicated by a ~35% decrease of $R_{S/N}$. In spring, $R_{S/N}$ were also lower at night,

290   by ~40% compared to the daytime results (Figure 5d). Given that the two campaigns showed

291   comparable discrepancies between the nighttime and daytime $R_{S/N}$, increase of vehicle emissions at

292   night was presumably not the dominant driver for the much stronger diurnal variations of MAE_{365}

293   observed in spring. Actually, MAE_{365} was almost independent of $R_{S/N}$ for the spring samples. For

294   example, the MAE_{365} values were found to fall into two well-separated ranges (above 2 and ~0.5–

295   1.5 m^2/gC, with the former observed only at night) for the samples with relatively low $R_{S/N}$ levels

296   (below 0.4), indicating that reduced $R_{S/N}$ was ineffective to explain the high MAE_{365} events

297   encountered in spring (Figure 5f). In addition to increased vehicle emissions at night, therefore,

298   there must exist other factors which were more responsible for the significant diurnal variations of

299   springtime MAE_{365}.

300   We first evaluated the influence of secondary aerosol formation. The spring campaign

301   experienced lower RH and substantially higher temperatures compared to winter, by ~25% and

302   30 °C, respectively. The springtime SOR were lower than the wintertime results (0.12 ± 0.06 vs.

303   0.15 ± 0.07), whereas an opposite pattern was observed for NOR (0.16 ± 0.08 vs. 0.12 ± 0.06). The

304   seasonal variations of SOR and NOR provided additional evidence for the inferences that the sulfate

305   and nitrate formation was more strongly contributed by heterogeneous and photochemical reactions,

306   respectively. For the spring campaign, the daytime and nighttime SOR were in general comparable

307   (Figure S1a) and no clear evidence was observed for the prevalence of heterogeneous chemistry,

308   presumably due to the rare occurrence of high RH conditions either during the day or at night.

309   Unlike SOR, the daytime NOR were considerably higher than the nighttime results (0.18 ± 0.09 vs.

310   0.14 ± 0.08; Figure S1b), pointing to enhanced photochemistry during the day. This pattern could

311   be partially responsible for the relatively low daytime MAE_{365}, since secondary brown carbon was

312   typically less light-absorbing than primary BrC (Kumar et al., 2018; Cappa et al., 2020; Ni et al.,

313   2021). However, MAE_{365} did not exhibit clear dependence on NOR or the nitrate to OC ratio (NO_3^-

314   /OC), e.g., the high MAE_{365} events were found to be associated with moderate NOR and NO_3^-/OC

315   levels (Figure S2). Thus for the spring campaign, photochemistry should not be the major

316   influencing factor for MAE_{365}, either.

317   We then investigated the role of biomass burning. Unlike the wintertime results, MAE_{365}

318   showed a strong positive correlation with LG/OC ($r = 0.84$) in spring (Figure 5e), suggesting

319   biomass burning emissions as the dominant driver for the variations of MAE_{365}. It is noteworthy

320   that the LG to OC ratios were substantially higher in spring than in winter, with averages of $3.11 \pm$

321   1.70% and $0.99 \pm 0.26\%$, respectively. This pattern could not be explained by seasonal variations in

322   residential consumption of biofuels, since April experienced much higher temperatures than January

323   (averaging 11 and -19 °C, respectively). Instead, the elevated springtime LG/OC should be

324 attributed primarily to open burning, as supported by the intensive fire hotspots detected around

325 Harbin in April (Figure 2b). The seasonal variations of LG to K^+ ratio (LG/K^+) also suggested that

326 the dominant burning ways were different between winter and spring. Compared to the relatively

327 small and constant LG/K^+ observed in January (0.46 ± 0.11), the ratios were nearly tripled in April

328 (1.28 ± 0.61) with more significant sample-by-sample differences (between ~0.5–3.5) (Figure 3b).

329 Recalling that the transition from flaming to smoldering combustion favored the increase of LG/K^+

330 (Gao et al., 2003), the springtime burning should have relatively low and variable combustion

331 efficiencies. This inference was in line with the fact that the agricultural fires were usually

332 uncontrolled, e.g., with respect to water content of crop residues and abundance of oxygen. In all,

333 for the spring campaign, the dominant driver for the variations of LG/OC and MAE_{365} could be

334 further identified as open burning. Subsequently, the higher LG/OC and MAE_{365} at night (Figures

335 5b–5c) could be attributed primarily to increased agricultural fires. The preference on nighttime

336 burning was not surprising, since the agricultural fires were illegal, i.e., nominally prohibited by the

337 Government of Heilongjiang Province.

338   It should be noted that the agricultural fire emissions increased LG/OC but had minimal

339 influence on $R_{S/N}$ (Figure S3). For example, the nighttime samples collected in spring differed

340 substantially with respect to the impact of agricultural fires, as indicated by their variable LG/OC

341 which spanned nearly one order of magnitude. However, no clear pattern was observed for $R_{S/N}$ with

342 increasing LG/OC, e.g., linear regression of $R_{S/N}$ on LG/OC showed an extremely low r value of

343 0.07.

344   The frequent occurrences of agricultural fires during April, 2021 to some extent masked the

345 "background" MAE_{365}, i.e., the value representative for the spring conditions without significant

346   influence of open burning. In spring, all the samples with LG/K$^+$ ratios of above one, i.e., a chemical

347   signature for apparent impacts of agricultural fires, were found to have LG/OC ratios larger than

348   2%. Thus in the following discussions, LG/OC of > 2% was used as an indicator for open burning

349   episodes and correspondingly, spring samples with LG/OC of below 2% were referred to as typical

350   ones. MAE$_{365}$ averaged 0.80 ±0.22 m^2/gC for the typical samples of spring, lower than results from

351   the winter campaign (1.55 ± 0.18 m^2/gC; Figure S4a). This seasonal pattern coincided with the

352   overall lower $R_{S/N}$ in spring (Figure S4b). It was unlikely that the number of in-use vehicles or the

353   fleet composition in Harbin could vary significantly between January and April of the same year.

354   Thus the reduced springtime $R_{S/N}$, i.e., the relatively low MAE$_{365}$ with the absence of agricultural

355   fires, should be caused mainly by the decrease of coal combustion emissions, e.g., due to the less

356   demand for heating.

357   **3.3 Unique wavelength dependence of BrC absorption during agricultural fire episodes**

358   The agricultural fires not only elevated MAE$_{365}$ but also changed the wavelength dependence

359   of brown carbon. For the wavelength range used for AAE calculation (310–460 nm), the detection

360   limit of optical attenuation (ATN$_{LOD}$) was ~0.02, which was determined as three times the maximum

361   standard deviation of parallel ATN$_\lambda$ results from blank filters. Before further discussions, we

362   introduced a new term "relative ln(ATN$_\lambda$)", i.e., ln(ATN$_\lambda$)* calculated as ln(ATN$_\lambda$) – ln(ATN$_{LOD}$).

363   A benefit of using the new term was that a ln(ATN$_\lambda$)* value of zero corresponded to ATN$_{LOD}$ and

364   thus could be interpreted independently, e.g., ATN$_{LOD}$ was independent of the sampling or analytical

365   procedures such as the volume of methanol used for extraction. It should be noted that the use of

366   ln(ATN$_\lambda$)* would not influence the determination of AAE, since the same slope would be derived

367   from the regressions of ln(ATN$_\lambda$)* and ln(ATN$_\lambda$) on ln(λ). For the typical samples of spring, the

368   dependence of $\ln(\text{ATN}_\lambda)^*$ on $\ln(\lambda)$ could be properly approximated by a linear function, usually with

369   r values of above 0.995. In this case, AAE could be reliably determined, and an average value of

370   6.92 ±0.28 was obtained.

371   The relationship between $\ln(\text{ATN}_\lambda)^*$ and $\ln(\lambda)$ became non-linear for the open burning episodes.

372   To more quantitatively describe the non-linearity, we added an "auxiliary line" to each measured

373   spectrum (Figure 6a), by drawing a line between the two points with x values of $\ln(310)$ and $\ln(460)$.

374   The "auxiliary line" could be considered an assumed spectrum with linear dependence of $\ln(\text{ATN}_\lambda)^*$

375   on $\ln(\lambda)$. The measured spectrum was always above the assumed one and their largest difference

376   was typically observed at ~365 nm, pointing to the presence of distinct BrC chromophores with

377   absorption peak around this wavelength.

378   The influence of such chromophores on BrC absorption could be estimated by the following

379   three indicators. The first one (F) was related to the difference between the measured and assumed

380    $\ln(\text{ATN}_\lambda)^*$ at 365 nm:

381    $F = \left[\ln\left(\text{ATN}_{365}\right)^*_m - \ln\left(\text{ATN}_{365}\right)^*_a \right] \Big/ \ln\left(\text{ATN}_{365}\right)^*_a$, where the subscripts "m" and "a" indicate

382   results from the measured and assumed spectra, respectively (Figure 6a). The second indicator (K)

383   was related to the area enclosed between the two spectra (S_2): $K = S_2/S_1$, where S_1 indicates the area

384   enclosed by the assumed spectrum and x-axis (Figure 6b). The last indicator was $\Delta(b_{abs})_{365}$

385   calculated as $\left(b_{abs}\right)^m_{365} - \left(b_{abs}\right)^a_{365}$, where the superscripts "m" and "a" indicate absorption

386   coefficients calculated based on the measured and assumed spectra, respectively. F and K exhibited

387   a strong linear correlation for the open burning episodes ($r = 0.99$; Figure 6c), indicating that the

388   differences between the measured and assumed spectra were likely caused by the same class of BrC

389   compounds. In addition, these compounds could be primarily traced back to biomass burning, since

Atmospheric
Chemistry
and Physics
Discussions

Open Access

EGU

390   $\Delta(b_{abs})_{365}$ showed a positive dependence on LG/OC (Figure 6d). A candidate for such compounds

391   was $C_7H_7NO_4$ (a methyl-substituted nitrocatechol), based on a synthesis of absorption spectra

392   measured for various BrC chromophores (Huang et al., 2020) and molecular characterization results

393   for biomass burning emissions (Lin et al., 2016, 2017; Xie et al., 2019, 2020). Chamber experiments

394   by Iinuma et al. (2010) suggested that $C_7H_7NO_4$ could also be formed through photooxidation of

395   gaseous precursors emitted by biomass burning (*m*-cresol). In this study, however, all the samples

396   with relatively high $\Delta(b_{abs})_{365}$ levels (e.g., above 20 Mm^{-1}) were collected at night, indicating that

397   the distinct BrC chromophores with absorption peak at ~365 nm (like $C_7H_7NO_4$) were more strongly

398   associated with primary emissions from agricultural fires. In addition, the chromophores seemed to

399   be subject to photo-bleaching, as both *F* and *K* decreased substantially (by ~65%) during the day

400   compared to the nighttime results (Figure 7).

401   For the open burning episodes, the distinct absorption peak at ~365 nm prohibited a proper

402   determination of AAE. If enforcing a linear function for the dependence of $\ln(ATN_\lambda)^*$ on $\ln(\lambda)$, lower

403   *r* values would be derived (down to ~0.97, with an average of 0.992 ±0.007) compared to the typical

404   samples (averaging 0.998 ±0.002). In addition, *r* showed a decreasing trend with the increase of

405   LG/OC (Figure 6e), suggesting that the relationship between $\ln(ATN_\lambda)^*$ and $\ln(\lambda)$ deviated more

406   significantly from linearity as the ~365 nm absorption peak, i.e., the influence of agricultural fires,

407   became more significant. We suggest that for the open burning episodes, the AAE results should be

408   interpreted with caution, although they could be calculated mathematically with reasonable *r* values

409   (e.g., even the minimum *r* appeared acceptable).

410   **3.4 Diurnal variations of wintertime AAE**

411   Similar to the typical samples of spring, $\ln(ATN_\lambda)^*$ exhibited linear dependences on $\ln(\lambda)$ for

412   all the winter samples. The wintertime AAE were higher at night compared to those observed during

413   the day (with averages of 7.33 $\pm$ 0.14 and 6.76 $\pm$ 0.11, respectively), consistent with the pattern

414   observed during winter in Beijing (Li et al., 2020). The relative abundance of secondary OC (SOC)

415   has been considered an important influencing factor for AAE, e.g., an increasing trend was observed

416   for AAE during long-range transport of BrC over the Indo-Gangetic Plain (Dasari et al., 2019).

417   Although SOC or its organic tracer was not determined in this study, previous source apportionment

418   results from Harbin (based on PMF) showed a strong correlation between SOC and sulfate, with

419   largely consistent relationships among different campaigns (Cheng et al., 2022b). Thus we used

420   sulfate as an indicator for SOC. During the winter campaign, the sulfate to OC ratios were lower at

421   night (averaging 0.38, compared to 0.44 during the day), pointing to decreased fractions of SOC in

422   OC. This inference was consistent with the higher LG/OC and $R_{S/N}$ levels observed at night, which

423   had been attributed to increased emissions from residential biomass burning and vehicular exhausts,

424   respectively. Thus regarding the association between AAE and SOC formation, results from the

425   winter campaign were inconsistent with Dasari et al. (2019), but the reason remained unclear.

426   Molecular characterization of organic aerosols should be necessary to unfold the response of AAE

427   to changes in BrC sources.

428   **4. Conclusions**

429   Diurnal variations of BrC were investigated during two distinct seasons in the northernmost

430   megacity in China. The winter campaign was characterized by low temperatures rarely seen in other

431   hotspots of air pollution studies such as the North China Plain. The wintertime BrC aerosols were

432   slightly more absorbing at night, with an average MAE_{365} of 1.61 $\pm$ 0.15 m^2/gC compared to 1.48 $\pm$

433   0.18 m^2/gC during the day. Various indicators were used to explain the observed diurnal variations

434 of MAE$_{365}$, including those associated with biomass burning emissions (LG/K$^+$ and LG/OC),

435 relative importance of coal combustion and vehicle emissions ($R_{S/N}$) and secondary aerosol

436 formation (SOR and NOR). For the winter campaign, the nighttime samples were characterized by

437 increased BB emissions from residential sources, enhanced heterogeneous chemistry and weakened

438 photochemical reactions. But none of these factors was identified as the dominant driver for the

439 higher MAE$_{365}$ at night. Instead, MAE$_{365}$ exhibited a negative dependence on $R_{S/N}$, and the lower

440 $R_{S/N}$ and thus higher MAE$_{365}$ at night were primarily attributed to increased emissions from heavy-

441 duty diesel trucks, which were not allowed for the main urban area during the day. In addition, the

442 wintertime AAE were higher at night but it remained difficult to unfold the underlying connection

443 between this diurnal pattern and the changes in BrC sources.

444 The spring campaign was characterized by frequent occurrences of agricultural fires, with more

445 pronounced diurnal variations of MAE$_{365}$ (averaging 0.98 ± 0.31 and 1.69 ± 0.65 m^2/gC for the

446 daytime and nighttime samples, respectively). Unlike winter, the springtime MAE$_{365}$ were mainly

447 influenced by open burning emissions, as suggested by the positive dependence of MAE$_{365}$ on

448 LG/OC and the lack of correlation between MAE$_{365}$ and $R_{S/N}$. The higher nighttime LG/OC

449 indicated that the farmers preferred burning the crop residues at night, presumably because

450 agricultural fires were nominally prohibited by the local government. In addition, BrC exhibited

451 distinct light absorption spectra during agricultural fire episodes, as indicated by the non-linear

452 relationship between ln(ATN$_\lambda$)* on ln(λ). The non-linearity was mainly caused by chromophores

453 with absorption peak at ~365 nm, which became more significant with increasing BB influence. A

454 candidate for the compounds at play was C$_7$H$_7$NO$_4$, based on a synthesis of absorption spectra

455 measured for various BrC chromophores and molecular measurement results for BB emissions. The

456   presence of such chromophores, i.e., the distinct absorption peak at ~365 nm, prohibited a proper

457   determination of AAE for the spring samples impacted by agricultural fires.

460   **Author contributions.** YC and JL designed the study and prepared the paper with inputs from all

461   the co-authors. XC, YZ and QY carried out the experiments. QZ and KH validated the results and

462   supervised the study.

463   **Competing interests.** Author Qiang Zhang is a member of the editorial board of *Atmospheric*

464   *Chemistry and Physics*. The peer-review process was guided by an independent editor, and the

465   authors have also no other competing interests to declare.

472   **References**

473   Akagi, S. K., Craven, J. S., Taylor, J. W., McMeeking, G. R., Yokelson, R. J., Burling, I. R., Urbanski,

474   S. P., Wold, C. E., Seinfeld, J. H., Coe, H., Alvarado, M. J., and Weise, D. R.: Evolution of

475   trace gases and particles emitted by a chaparral fire in California, *Atmos. Chem. Phys.*, 12,

476   1397–1421, https://doi.org/10.5194/acp-12-1397-2012, 2012.

477   Brege, M. A., China, S., Schum, S., Zelenyuk, A., and Mazzoleni, L. R.: Extreme molecular

478   complexity resulting in a continuum of carbonaceous species in biomass burning tar balls from

479   wildfire smoke, *ACS Earth Space Chem.*, 5, 2729–2739,

480   https://doi.org/10.1021/acsearthspacechem.1c00141, 2015.

Atmospheric
Chemistry
and Physics
Discussions

Open Access

EGU

481   Brown, H., Liu, X. H., Feng, Y., Jiang, Y. Q., Wu, M. X., Lu, Z., Wu, C. L., Murphy, S., and Pokhrel,
482   R.: Radiative effect and climate impacts of brown carbon with the Community Atmosphere
483   Model (CAM5), *Atmos. Chem. Phys.*, 18, 17745–17768, https://doi.org/10.5194/acp-18-
484   17745-2018, 2018.

485   Cappa, C. D., Lim, C. Y., Hagan, D. H., Coggon, M., Koss, A., Sekimoto, K., de Gouw, J., Onasch,
486   T. B., Warneke, C., and Kroll, J. H.: Biomass-burning-derived particles from a wide variety of
487   fuels – Part 2: effects of photochemical aging on particle optical and chemical properties,
488   *Atmos. Chem. Phys.*, 20, 8511–8532, https://doi.org/10.5194/acp-20-8511-2020, 2020.

489   Chen, X. R., Wang, H. C., Lu, K. D., Li, C. M., Zhai, T. Y., Tan, Z. F., Ma, X. F., Yang, X. P., Liu,
490   Y. H., Chen, S. Y., Dong, H. B., Li, X., Wu, Z. J., Hu, M., Zeng, L. M., and Zhang, Y. H.: Field
491   determination of nitrate formation pathway in winter Beijing, *Environ. Sci. Technol.*, 54,
492   9243–9253, https://doi.org/10.1021/acs.est.0c00972, 2020.

493   Chen, Y., and Bond, T. C.: Light absorption by organic carbon from wood combustion, *Atmos.*
494   *Chem. Phys.*, 10, 1773–1787, https://doi.org/10.5194/acp-10-1773-2010, 2010.

495   Cheng, Y.: Data for Measurement report: Diurnal variations of brown carbon during two distinct
496   seasons in a megacity in Northeast China [data set], https://doi.org/10.5281/zenodo.7590785,
497   2023.

498   Cheng, Y., He, K. B., Du, Z. Y., Engling, G., Liu, J. M., Ma, Y. L., Zheng, M., and Weber, R. J.: The
499   characteristics of brown carbon aerosol during winter in Beijing, *Atmos. Environ.*, 127, 355–
500   364, https://doi.org/10.1016/j.atmosenv.2015.12.035, 2016.

501   Cheng, Y., Cao, X. B., Liu, J. M., Yu, Q. Q., Wang, P., Yan, C. Q., Du, Z. Y., Liang, L. L., Zhang,
502   Q., and He, K. B.: Primary nature of brown carbon absorption in a frigid atmosphere with
503   strong haze chemistry, Environ. Res., 204, 112324,
504   https://doi.org/10.1016/j.envres.2021.112324, 2022a.

505   Cheng, Y., Cao, X. B., Liu, J. M., Yu, Q. Q., Zhong, Y. J., Geng, G. N., Zhang, Q., and He, K. B.:
506   New open burning policy reshaped the aerosol characteristics of agricultural fire episodes in
507   Northeast China, *Sci. Total Environ.*, 810, 152272,
508   https://doi.org/10.1016/j.scitotenv.2021.152272, 2022b.

509   Chu, B. W., Zhang, S. P., Liu, J., Ma, Q. X., and He, H.: Significant concurrent decrease in $PM_{2.5}$
510   and NO_2 concentrations in China during COVID-19 epidemic, *J. Environ. Sci.*, 99, 346–353,
511   https://doi.org/10.1016/j.jes.2020.06.031, 2021.

512   Dallmann, T. R., DeMartini, S. J., Kirchstetter, T. W., Herndon, S. C., Onasch, T. B., Wood, E. C.,
513   and Harley, R. A.: On-road measurement of gas and particle phase pollutant emission factors

514   for individual heavy-duty diesel trucks, *Environ. Sci. Technol.*, 46, 8511–8518,
515   https://doi.org/10.1021/es301936c, 2012.

516 Dasari, S., Andersson, A., Bikkina, S., Holmstrand, H., Budhavant, K., Satheesh, S., Asmi, E., Kesti,
517   J., Backman, J., Salam, A., Bisht, D. S., Tiwari, S., Hameed, Z., and Gustafsson, Ö.:
518   Photochemical degradation affects the light absorption of water-soluble brown carbon in the
519   South Asian outflow, *Sci. Adv.*, 5, eaau8066, https://doi.org/10.1126/sciadv.aau8066, 2019.

520 Du, W., Shen, G. F., Chen, Y. C., Zhu, X., Zhuo, S. J., Zhong, Q. R., Qi, M., Xue, C. Y., Liu, G. Q.,
521   Zeng, E., Xing, B. S., and Tao, S.: Comparison of air pollutant emissions and household air
522   quality in rural homes using improved wood and coal stoves, *Atmos. Environ.*, 166, 215–223,
523   https://doi.org/10.1016/j.atmosenv.2017.07.029, 2017.

524 Engling, G., Carrico, C. M., Kreidenweis, S. M., Collett Jr., J. L., Day, D. E., Malm, W. C., Lincoln,
525   L., Hao, W. M., Iinuma, Y., and Herrmann, H.: Determination of levoglucosan in biomass
526   combustion aerosol by high-performance anion-exchange chromatography with pulsed
527   amperometric detection, *Atmos. Environ.*, 40, S299–S311,
528   https://doi.org/10.1016/j.atmosenv.2005.12.069, 2006.

529 Gao, S., Hegg, D. A., Hobbs, P. V., Kirchstetter, T. W., Magi, B. I., and Sadilek, M.: Water-soluble
530   organic components in aerosols associated with savanna fires in southern Africa: identification,
531   evolution, and distribution, *J. Geophys. Res.*, 108, D13, 8491,
532   https://doi.org/10.1029/2002JD002324, 2003.

533 Hecobian, A., Zhang, X., Zheng, M., Frank, N., Edgerton, E. S., and Weber, R. J.: Water-soluble
534   organic aerosol material and the light-absorption characteristics of aqueous extracts measured
535   over the Southeastern United States, *Atmos. Chem. Phys.*, 10, 5965–5977,
536   https://doi.org/10.5194/acp-10-5965-2010, 2010.

537 Huang, R. J., Yang, L., Shen, J .C., Yuan, W., Gong, Y. Q., Guo, J., Cao, W. J., Duan, J., Ni, H. Y.,
538   Zhu, C. S., Dai, W. T., Li, Y. J., Chen, Y., Chen, Q., Wu, Y. F., Zhang, R. J., Dusek, U., and
539   O'Dowd, C.: Water-Insoluble organics dominate brown carbon in wintertime urban aerosol of
540   China: chemical characteristics and optical properties, *Environ. Sci. Technol.*, 54, 7836–7847,
541   https://doi.org/10.1021/acs.est.0c01149, 2020.

542 Huang, R. J., Yang, L., Shen, J. C., Yuan, W., Gong, Y. Q., Ni, H. Y., Duan, J., Yan, J., Huang, H.
543   B., You, Q. H., and Li, Y. J.: Chromophoric fingerprinting of brown carbon from residential
544   biomass burning, *Environ. Sci. Technol. Lett.*, 9, 102–111,
545   https://doi.org/10.1021/acs.estlett.1c00837, 2022.

546 Huo, Y. Q., Guo, Z. H., Li, Q., Wu, D., Ding, X., Liu, A. L., Huang, D., Qiu, G. K., Wu, M. M.,
547   Zhao, Z. J., Sun, H., Song, W. H., Li, X., Chen, Y. J., Wu, T. C., and Chen, J. M.: Chemical

548   fingerprinting of HULIS in particulate matters emitted from residential coal and biomass
549   combustion, *Environ. Sci. Technol.*, 55, 3593–3603,
550   https://doi.org/10.1021/acs.est.0c08518, 2021.

551   Iinuma, Y., Böge, O., Gräfe, R., and Herrmann, H.: Methyl-nitrocatechols: atmospheric tracer
552   compounds for biomass burning secondary organic aerosols, *Environ. Sci. Technol.*, 44, 8453–
553   8459, https://doi.org/10.1021/es102938a, 2010.

554   Jiang, H. X., Li, J., Sun, R., Tian, C. G., Tang, J., Jiang, B., Liao, Y. H., Chen, C. E., and Zhang, G.:
555   Molecular dynamics and light absorption properties of atmospheric dissolved organic matter,
556   *Environ. Sci. Technol.*, 55, 10268–10279, https://doi.org/10.1021/acs.est.1c01770, 2021.

557   Kumar, N. K., Corbin, J. C., Bruns, E. A., Massabó, D., Slowik, J. G., Drinovec, L., Močnik, G.,
558   Prati, P., Vlachou, A., Baltensperger, U., Gysel, M., El-Haddad, I., and Prévôt, A. S. H.:
559   Production of particulate brown carbon during atmospheric aging of residential wood-burning
560   emissions, *Atmos. Chem. Phys.*, 18, 17843–17861, https://doi.org/10.5194/acp-18-17843-
561   2018, 2018.

562   Lack, D. A., Langridge, J. M., Bahreini, R., Cappa, C. D., Middlebrook, A. M., and Schwarz, J. P.:
563   Brown carbon and internal mixing in biomass burning particles, *Proc. Natl. Acad. Sci. USA*,
564   109, 14802–14807, https://doi.org/10.1073/pnas.1206575109, 2012.

565   Laskin, A., Laskin, J., and Nizkorodov, S. A.: Chemistry of atmospheric brown carbon, *Chem. Rev.*,
566   115, 4335–4382, https://doi.org/10.1021/cr5006167, 2015.

567   Li, M., Liu, H., Geng, G. N., Hong, C. P., Liu, F., Song, Y., Tong, D., Zheng, B., Cui, H. Y., Man,
568   H. Y., Zhang, Q., and He, K. B.: Anthropogenic emission inventories in China: a review, *Natl.*
569   *Sci. Rev.*, 4, 834–866, https://doi.org/10.1093/nsr/nwx150, 2017.

570   Li, X., Wang, Y. J., Hu, M., Tan, T. Y., Li, M. R., Wu, Z. J., Chen, S. Y., and Tang, X. Y.:
571   Characterizing chemical composition and light absorption of nitroaromatic compounds in the
572   winter of Beijing, *Atmos. Environ.*, 237, 117712,
573   https://doi.org/10.1016/j.atmosenv.2020.117712, 2019.

574   Li, Y. C., Liu, J., Han, H., Zhao, T. L., Zhang, X., Zhuang, B. L., Wang, T. J., Chen, H. M., Wu, Y.,
575   and Li, M. M.: Collective impacts of biomass burning and synoptic weather on surface $PM_{2.5}$
576   and CO in Northeast China, *Atmos. Environ.*, 213, 64–80,
577   https://doi.org/10.1016/j.atmosenv.2019.05.062, 2019.

578   Li, Y. R., Tan, Z. Q., Ye, C. X., Wang, J. X., Wang, Y. W., Zhu, Y., Liang, P. F., Chen, X., Fang, Y.
579   H., Han, Y. Q., Wang, Q., He, D., Wang, Y., and Zhu, T.: Using wavelet transform to analyse
580   on-road mobile measurements of air pollutants: a case study to evaluate vehicle emission

581   control policies during the 2014 APEC summit, *Atmos. Chem. Phys.*, 19, 13841–13857,
582   https://doi.org/10.5194/acp-19-13841-2019, 2019.

583 Lian, X. B., Huang, J. P., Huang, R. J., Liu, C. W., Wang, L. N., and Zhang, T. H.: Impact of city
584   lockdown on the air quality of COVID-19-hit of Wuhan city, *Sci. Total Environ.*, 742, 140556,
585   https://doi.org/10.1016/j.scitotenv.2020.140556, 2020.

586 Lin, P., Aiona, P. K., Li, Y., Shiraiwa, M., Laskin, J., Nizkorodov, S. A., and Laskin, A.: Molecular
587   characterization of brown carbon in biomass burning aerosol particles, *Environ. Sci. Technol.*,
588   50, 11815–11824, https://doi.org/10.1021/acs.est.6b03024, 2016.

589 Lin, P., Bluvshtein, N., Rudich, Y., Nizkorodov, S. A., Laskin, J., and Laskin, A.: Molecular
590   chemistry of atmospheric brown carbon inferred from a nationwide biomass burning event,
591   *Environ. Sci. Technol.*, 51, 11561–11570, https://doi.org/10.1021/acs.est.7b02276, 2017.

592 Lin, P., Fleming, L. T., Nizkorodov, S. A., Laskin, J., and Laskin, A.: Comprehensive molecular
593   characterization of atmospheric brown carbon by high resolution mass spectrometry with
594   electrospray and atmospheric pressure photoionization, *Anal. Chem.*, 90, 12493–12502,
595   https://doi.org/10.1021/acs.analchem.8b02177, 2018.

596 Lin, P., Laskin, J., Nizkorodov, S. A., and Laskin, A.: Revealing brown carbon chromophores
597   produced in reactions of methylglyoxal with ammonium sulfate, *Environ. Sci. Technol.*, 49,
598   14257–14266, https://doi.org/10.1021/acs.est.5b03608, 2015.

599 Liu, T. Y., Chan, A. W. H., and Abbatt, J. P. D.: Multiphase oxidation of sulfur dioxide in aerosol
600   particles: implications for sulfate formation in polluted environments, *Environ. Sci. Technol.*,
601   8, 4227–4242, https://doi.org/10.1021/acs.est.0c06496, 2021.

602 Liu, X. X., Zhang, Y., Huey, L. G., Yokelson, R. J., Wang, Y., Jimenez, J. L., Campuzano-Jost, P.,
603   Beyersdorf, A. J., Blake, D. R., Choi, Y., St Clair, J. M., Crounse, J. D., Day, D. A., Diskin, G.
604   S., Fried, A., Hall, S. R., Hanisco, T. F., King, L. E., Meinardi, S., Mikoviny, T., Palm, B. B.,
605   Peischl, J., Perring, A. E., Pollack, I. B., Ryerson, T. B., Sachse, G., Schwarz, J. P., Simpson, I.
606   J., Tanner, D. J., Thornhill, K. L., Ullmann, K., Weber, R. J., Wennberg, P. O., Wisthaler, A.,
607   Wolfe, G. M., and Ziemba, L. D.: Agricultural fires in the southeastern U.S. during SEAC[4]RS:
608   emissions of trace gases and particles and evolution of ozone, reactive nitrogen, and organic
609   aerosol, *J. Geophys. Res. Atmos.*, 121, 7383–7414, https://doi.org/10.1002/2016JD025040,
610   2016.

611 McClure, C. D., Lim, C. Y., Hagan, D. H., Kroll, J. H., and Cappa, C. D.: Biomass-burning-derived
612   particles from a wide variety of fuels – Part 1: properties of primary particles, *Atmos. Chem.*
613   *Phys.*, 20, 1531–1547, https://doi.org/10.5194/acp-20-1531-2020, 2020.

Atmospheric
Chemistry
and Physics
Discussions

McMeeking, G. R., Kreidenweis, S. M., Baker, S., Carrico, C. M., Chow, J. C., Collett Jr., J. L., Hao, W. M., Holden, A. S., Kirchstetter, T. W., Malm, W. C., Moosmüller, H., Sullivan, A. P., and Wold, C. E.: Emissions of trace gases and aerosols during the open combustion of biomass in the laboratory, *J. Geophys. Res.*, 114, D19210, https://doi.org/10.1029/2009JD011836, 2009.

Mohr, C., Lopez-Hilfiker, F. D., Zotter, P., Prévôt, A. S. H., Xu, L., Ng, N. L., Herndon, S. C., Williams, L. R., Franklin, J. P., Zahniser, M. S., Worsnop, D. R., Knighton, W. B., Aiken, A. C., Gorkowski, K. J., Dubey, M. K., Allan, J. D., and Thornton, J. A.: Contribution of nitrated phenols to wood burning brown carbon light absorption in Detling, United Kingdom during winter time, *Environ. Sci. Technol.*, 47, 6316–6324, https://doi.org/10.1021/es400683v, 2013.

Ni, H. Y., Huang, R. J., Pieber, S. M., Corbin, J. C., Stefenelli, G., Pospisilova, V., Klein, F., Gysel-Beer, M., Yang, L., Baltensperger, U., El Haddad, I., Slowik, J. G., Cao, J. J., Prévôt, A. S. H., and Dusek, U.: Brown carbon in primary and aged coal combustion emission, *Environ. Sci. Technol.,* 55, 5701–5710, https://doi.org/10.1021/acs.est.0c08084, 2021.

Pokhrel, R. P., Wagner, N. L., Langridge, J. M., Lack, D. A., Jayarathne, T., Stone, E. A., Stockwell, C. E., Yokelson, R. J., and Murphy, S. M.: Parameterization of single-scattering albedo (SSA) and absorption Ångström exponent (AAE) with EC/OC for aerosol emissions from biomass burning, *Atmos. Chem. Phys.*, 16, 9549–9561, https://doi.org/10.5194/acp-16-9549-2016, 2016.

Saleh, R.: From measurements to models: toward accurate representation of brown carbon in climate calculations, *Curr. Pollut. Rep.*, 6, 90–104, https://doi.org/10.1007/s40726-020-00139-3, 2020.

Salvador, C. M. G., Tang, R. Z., Priestley, M., Li, L. J., Tsiligiannis, E., Le Breton, M., Zhu, W. F., Zeng, L. M., Wang, H., Yu, Y., Hu, M., Guo, S., and Hallquist, M.: Ambient nitro-aromatic compounds – biomass burning versus secondary formation in rural China, *Atmos. Chem. Phys.*, 21, 1389–1406, https://doi.org/10.5194/acp-21-1389-2021, 2021.

Sand, M., Samset, B. H., Myhre, G., Gliβ, J., Bauer, S. E., Bian, H. S., Chin, M., Checa-Garcia, R., Ginoux, P., Kipling, Z., Kirkevåg, A., Kokkola, H., Le Sager, P., Lund, M. T., Matsui, H., van Noije, T., Olivié, D. J. L., Remy, S., Schulz, M., Stier, P., Stjern, C. W., Takemura, T., Tsigaridis, K., Tsyro, S. G., and Watson-Parris, D.: Aerosol absorption in global models from AeroCom phase III, *Atmos. Chem. Phys.*, 21, 15929–15947, https://doi.org/10.5194/acp-21-15929-2021, 2021.

Shen, X. B., Hao, J. T., Kong, L., Shi, Y., Cao, X. Y., Shi, J. C., Yao, Z. L., Li, X., Wu, B. B., Xu, Y. M., and He, K. B.: Variation characteristics of fine particulate matter and its components in diesel vehicle emission plumes, *J. Environ. Sci.*, 107, 138–149, https://doi.org/10.1016/j.jes.2021.01.034, 2021.

Atmospheric
Chemistry
and Physics
Discussions

648 Su, H., Cheng, Y. F., and Pöschl, U.: New multiphase chemical processes influencing atmospheric
649   aerosols, air quality, and climate in the Anthropocene, *Acc. Chem. Res.*, 53, 2034–2043,
650   https://doi.org/10.1021/acs.accounts.0c00246, 2020.

651 Tabazadeh, A., Djikaev, Y. S., and Reiss, H.: Surface crystallization of supercooled water in clouds,
652   *Proc. Natl. Acad. Sci. USA*, 99, 15873–15878, https://doi.org/10.1073/pnas.252640699, 2002.

653 Wang, Q. Q., Zhou, Y. Y., Ma, N., Zhu, Y., Zhao, X. C., Zhu, S. W., Tao, J. C., Hong, J., Wu, W. J.,
654   Cheng, Y. F., and Su, H.: Review of brown carbon aerosols in China: pollution level, optical
655   properties, and emissions, *J. Geophys. Res. Atmos.*, 127, e2021JD035473,
656   https://doi.org/10.1029/2021JD035473, 2022.

657 Wang, Y. S., Li, W. J., Gao, W. K., Liu, Z. R., Tian, S. L., Shen, R. R., Ji, D. S., Wang, S., Wang, L.
658   L., Tang, G. Q., Song, T., Cheng, M. T., Wang, G. H., Gong, Z. Y., Hao, J. M., and Zhang, Y.
659   H.: Trends in particulate matter and its chemical compositions in China from 2013-2017, *Sci.*
660   *China Earth Sci.*, 62, 1857–1871, https://doi.org/10.1007/s11430-018-9373-1, 2019.

661 Washenfelder, R. A., Azzarello, L., Ball, K., Brown, S. S., Decker, Z. C. J., Franchin, A.,
662   Fredrickson, C. D., Hayden, K., Holmes, C. D., Middlebrook, A. M., Palm, B. B., Pierce, R.
663   B., Price, D. J., Roberts, J. M., Robinson, M. A., Thornton, J. A., Womack, C. C., and Young,
664   C. J.: Complexity in the evolution, composition, and spectroscopy of brown carbon in aircraft
665   measurements of wildfire plumes, *Geophys. Res. Lett.*, 49, e2022GL098951,
666   https://doi.org/10.1029/2022GL098951, 2022.

667 Wozniak, A. S., Bauer, J. E., Sleighter, R. L., Dickhut, R. M., and Hatcher, P. G.: Technical Note:
668   Molecular characterization of aerosol-derived water soluble organic carbon using ultrahigh
669   resolution electrospray ionization Fourier transform ion cyclotron resonance mass
670   spectrometry, *Atmos. Chem. Phys.*, 8, 5099–5111, https://doi.org/10.5194/acp-8-5099-2008,
671   2008.

672 Wu, J., Kong, S. F., Yan, Y. Y., Yao, L. Q., Yan, Q., Liu, D. T., Shen, G. F., Zhang, X. Y., and Qi, S.
673   H.: Neglected biomass burning emissions of air pollutants in China-views from the corncob
674   burning test, emission estimation, and simulations, *Atmos. Environ.*, 278, 119082,
675   https://doi.org/10.1016/j.atmosenv.2022.119082, 2022.

676 Xie, M. J., Chen, X., Hays, M. D., and Holder, A. L.: Composition and light absorption of N-
677   containing aromatic compounds in organic aerosols from laboratory biomass burning, *Atmos.*
678   *Chem. Phys.*, 19, 2899–2915, https://doi.org/10.5194/acp-19-2899-2019, 2019.

679 Xie, M. J., Zhao, Z. Z., Holder, A. L., Hays, M. D., Chen, X., Shen, G. F., Jetter, J. J., Champion,
680   W. M., and Wang, Q. G.: Chemical composition, structures, and light absorption of N-
681   containing aromatic compounds emitted from burning wood and charcoal in household

682 cookstoves, *Atmos. Chem. Phys.*, 20, 14077–14090, https://doi.org/10.5194/acp-20-14077-
683 2020, 2020.

684 Xu, J. Z., Hettiyadura, A. P. S., Liu, Y. M., Zhang, X. H., Kang, S. C., and Laskin, A.: Atmospheric
685 brown carbon on the Tibetan Plateau: regional differences in chemical composition and light
686 absorption properties, *Environ. Sci. Technol. Lett.*, 9, 219−225,
687 https://doi.org/10.1021/acs.estlett.2c00016, 2022.

688 Yang, M., Howell, S. G., Zhuang, J., and Huebert, B. J.: Attribution of aerosol light absorption to
689 black carbon, brown carbon, and dust in China - Interpretations of atmospheric measurements
690 during EAST-AIRE, *Atmos. Chem. Phys.*, 9, 2035–2050, https://doi.org/10.5194/acp-9-2035-
691 2009, 2009.

692 Yttri, K. E., Schnelle-Kreis, J., Maenhaut, W., Abbaszade, G., Alves, C., Bjerke, A., Bonnier, N.,
693 Bossi, R., Claeys, M., Dye, C., Evtyugina, M., Garcń-Gacio, D., Hillamo, R., Hoffer, A., Hyder,
694 M., Iinuma, Y., Jaffrezo, J. L., Kasper-Giebl, A., Kiss, G., Lopez-Mahia, P. L., Pio, C., Piot, C.,
695 Ramirez-Santa-Cruz, C., Sciare, J., Teinilä, K., Vermeylen, R., Vicente, A., and Zimmermann,
696 R.: An intercomparison study of analytical methods used for quantification of levoglucosan in
697 ambient aerosol filter samples, *Atmos. Meas. Tech.*, 8, 125–147, https://doi.org/10.5194/amt-
698 8-125-2015, 2015.

699 Yuan, Q., Qi, B., Hu, D. Y., Wang, J. J., Zhang, J., Yang, H. Q., Zhang, S. S., Liu, L., Xu, L., and Li,
700 W. J.: Spatiotemporal variations and reduction of air pollutants during the COVID-19
701 pandemic in a megacity of Yangtze River Delta in China, *Sci. Total Environ.*, 751, 141820,
702 https://doi.org/10.1016/j.scitotenv.2020.141820, 2021.

703 Zeng, L. H., Dibb, J., Scheuer, E., Katich, J. M., Schwarz, J. P., Bourgeois, I., Peischl, J., Ryerson,
704 T., Warneke, C., Perring, A. E., Diskin, G. S., DiGangi, J. P., Nowak, J. B., Moore, R. H.,
705 Wiggins, E. B., Pagonis, D., Guo, H. Y., Campuzano-Jost, P., Jimenez, J. L., Xu, L., and Weber,
706 R. J.: Characteristics and evolution of brown carbon in western United States wildfires, *Atmos.*
707 *Chem. Phys.*, 22, 8009–8036, https://doi.org/10.5194/acp-22-8009-2022, 2022.

708 Zeng, L. H., Zhang, A. X., Wang, Y. H., Wagner, N. L., Katich, J. M., Schwarz, J. P., Schill, G. P.,
709 Brock, C., Froyd, K. D., Murphy, D. M., Williamson, C. J., Kupc, A., Scheuer, E., Dibb, J., and
710 Weber, R. J.: Global measurements of brown carbon and estimated direct radiative effects,
711 *Geophys. Res. Lett.*, 47, e2020GL088747, https://doi.org/10.1029/2020GL088747, 2020.

712 Zeng, Y. L., Ning, Y. L., Shen, Z. X., Zhang, L. M., Zhang, T., Lei, Y. L., Zhang, Q., Li, G. H., Xu,
713 H. M., Ho, S. S. H., and Cao, J. J.: The roles of N, S, and O in molecular absorption features
714 of brown carbon in $PM_{2.5}$ in a typical semi-arid megacity in Northwestern China, *J. Geophys.*
715 *Res. Atmos.*, 126, e2021JD034791, https://doi.org/10.1029/2021JD034791, 2021.

716 Zhang, J., Smith, K. R., Ma, Y., Ye, S., Jiang, F., Qi, W., Liu, P., Khalil, M. A. K., Rasmussen, R.
717   A., and Thorneloe, S. A.: Greenhouse gases and other airborne pollutants from household
718   stoves in China: a database for emission factors, *Atmos. Environ.*, 34, 4537–4549,
719   https://doi.org/10.1016/S1352-2310(99)00450-1, 2000.

720 Zhang, Y. L., Wang, X. M., Li, G. H., Yang, W. Q., Huang, Z. H., Zhang, Z., Huang, X. Y., Deng,
721   W., Liu, T. Y., Huang, Z. Z., and Zhang, Z. Y.: Emission factors of fine particles, carbonaceous
722   aerosols and traces gases from road vehicles: recent tests in an urban tunnel in the Pearl River
723   Delta, China, *Atmos. Environ.*, 122, 876–884, https://doi.org/10.1016/j.atmosenv.2015.08.024,
724   2015.
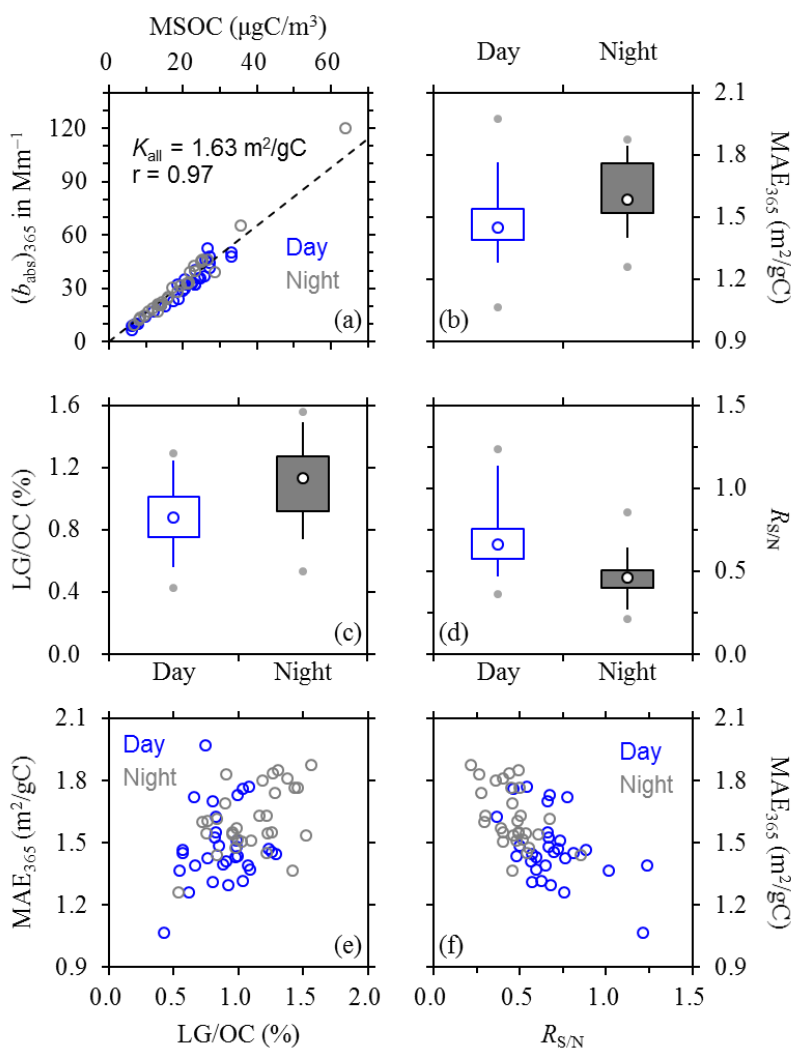
Figure 1. (a) Dependence of $(b_{abs})_{365}$ on MSOC, **(b–d)** diurnal variations of MAE_{365}, LG/OC (on a basis of carbon mass) and $R_{S/N}$, and **(e–f)** dependences of MAE_{365} on LG/OC or $R_{S/N}$ during winter. In (a), the dashed line indicates linear regression result based on all the winter samples, with K_{all} as slope (intercept was set as zero). In (b-d), lower and upper box bounds indicate the 25th and 75th percentiles, the whiskers below and above the box indicate the 5th and 95th percentiles, the solid circles below and above the box indicate the minimum and maximum, and the open circle within the box marks the median (the same hereinafter). Comparison of (e) and (f) suggests that the wintertime MAE_{365} was more strongly influenced by $R_{S/N}$ compared to LG/OC. The dependence shown in (f) could be approximated by the following function for all the winter samples ($r = 0.61$): $MAE_{365} = (-0.51 \pm 0.09) \times R_{S/N} + (1.84 \pm 0.05)$.
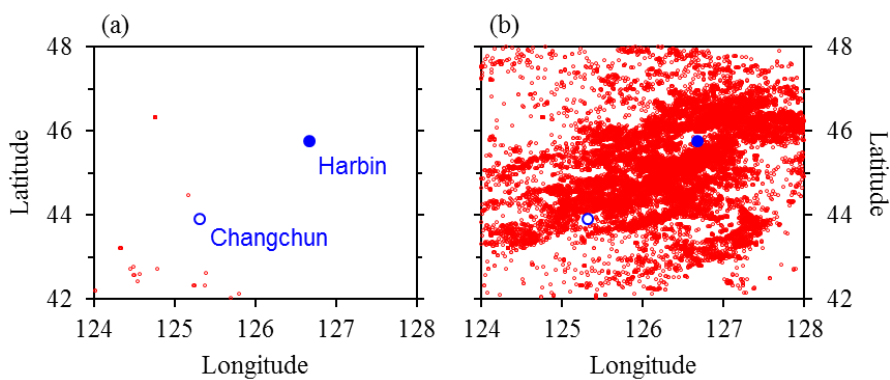
**Figure 2.** Active fires (red circles) detected during the **(a)** winter and **(b)** spring measurement periods around Harbin. The location of another central city of the HC metropolitan area, Changchun, is also shown. The fire data were based on the joint NASA/NOAA Suomi National Polar-orbiting Partnership (S-NPP) satellite, and were downloaded from the Fire Information for Resource Management System (FIRMS; https://firms.modaps.eosdis.nasa.gov/, last access: 1 January, 2023).
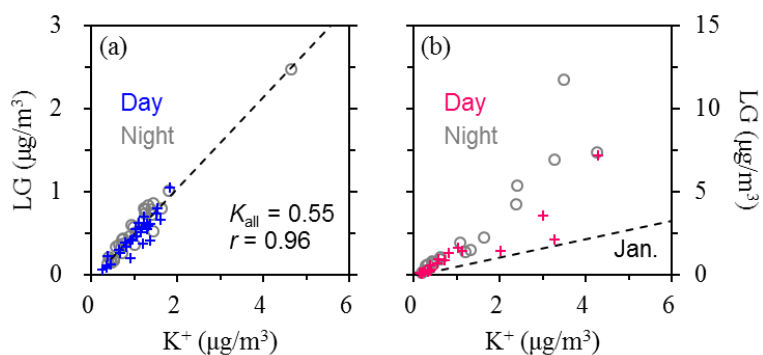
Figure 3. Dependences of levoglucosan on K^+ during **(a)** winter and **(b)** spring. In (a), the dashed line indicates linear regression result based on all the winter samples, with K_{all} as slope. The regression line of winter campaign is also shown in (b) for comparison to highlight the increased and variable LG/K^+ ratios in spring. The relatively low and constant LG/K^+ in winter were attributed to residential burning of crop residues, a routine activity occurring every day in rural areas for cooking and heating. The higher LG/K^+ in spring were associated with agricultural fires, as supported by the intensive fire hotspots detected.

750
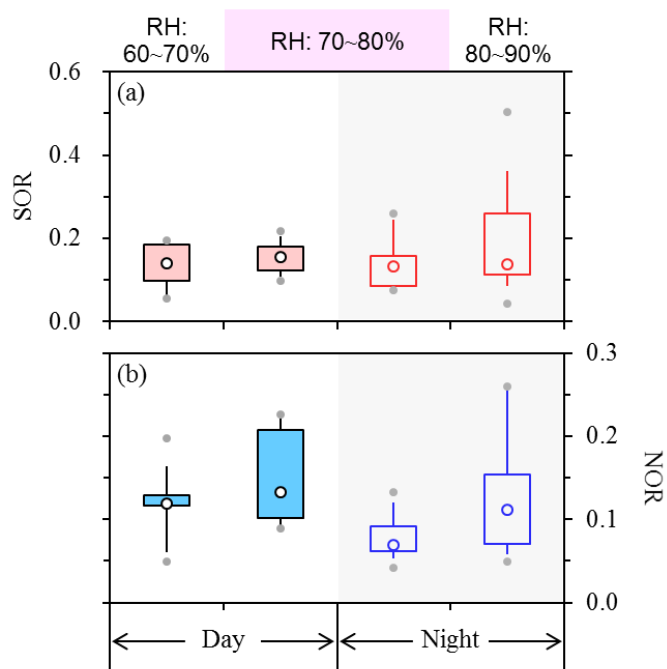
Figure 4. Diurnal variations of **(a)** SOR and **(b)** NOR in winter, with results from different RH
ranges shown separately. Daytime and nighttime samples had the same RH range of 70–80%,
whereas low RH levels of 60–70% and high RH levels of 80–90% occurred only during the day and
at night, respectively.
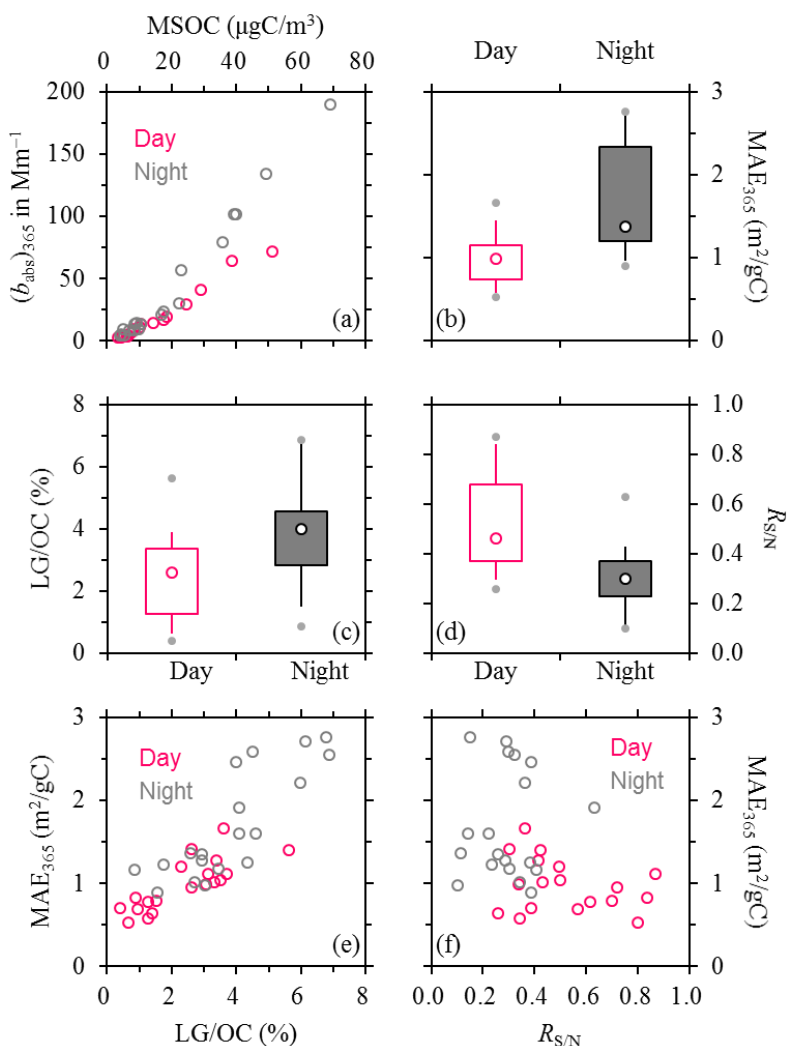
Figure 5. The same as Figure 1 but for spring. MAE_{365} showed more pronounced diurnal variations in spring than winter, although the daytime vs. nighttime discrepancies in $R_{S/N}$ were comparable between the two seasons. Comparison of (e) and (f) suggests that unlike winter, the springtime MAE_{365} was more strongly influenced by LG/OC than by $R_{S/N}$. The dependence shown in (e) could be approximated by the following function for all the spring samples ($r = 0.84$): $MAE_{365} = (30.48 \pm 3.28) \times LG/OC + (0.39 \pm 0.12)$.
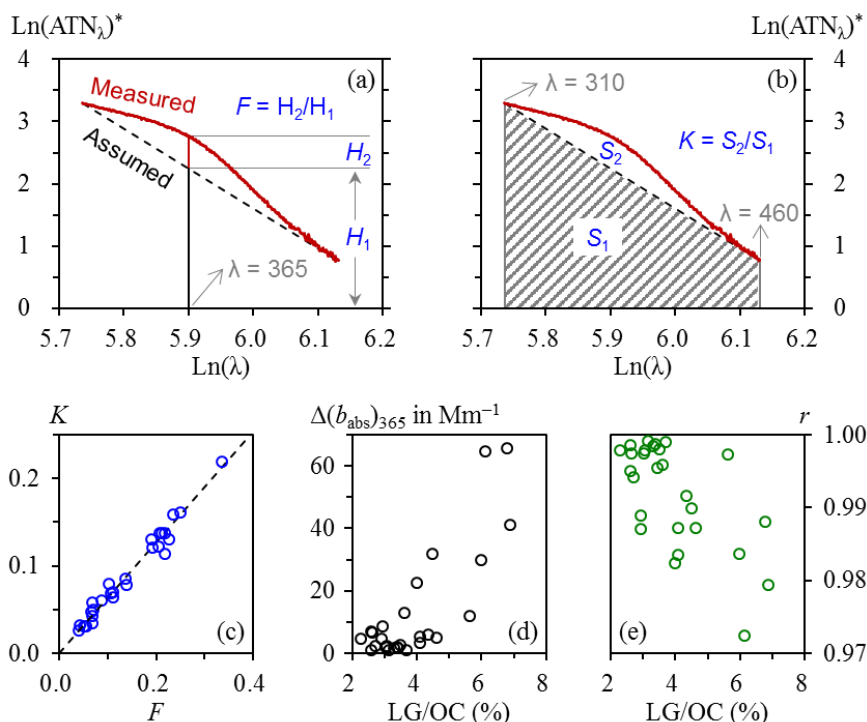
Figure 6. Nonlinearity of $\ln(ATN_\lambda)^*$ on $\ln(\lambda)$ during agricultural fire episodes in spring: **(a–b)** illustrations of the determination of F and K, **(c)** comparison of K and F, and **(d–e)** dependences of $\Delta(b_{abs})_{365}$ and r on LG/OC. In (a) and (b), the measured spectrum correspond to the nighttime sample collected on April 21, 2021, which had an LG/OC of 6.87%; the assumed spectrum was generated by drawing a line between the two points with x values of $\ln(310)$ and $\ln(460)$; H_1 indicates $\ln(ATN_{365})^*$ of the assumed spectrum, while H_2 indicates the difference in $\ln(ATN_{365})^*$ between the two spectra; S_1 indicates the area enclosed by the assumed spectrum and the x-axis, while S_2 indicates the area enclosed between the two spectra. In (c), the dashed line indicates linear regression result (intercept was set as zero) and the corresponding r value was 0.99. In (e), r was derived from linear regression of $\ln(ATN_\lambda)^*$ on $\ln(\lambda)$. Although the r values seemed reasonable, the AAE results should be interpreted with caution given the apparent absorption peak at ~365 nm.
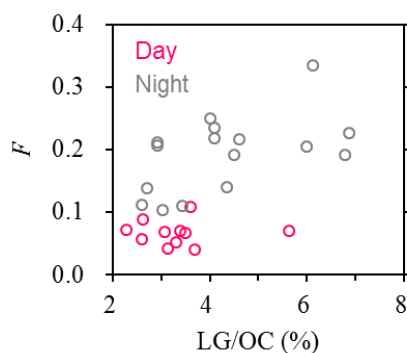
Figure 7. Dependence of F, a measure of the significance of the ~365 nm absorption peak, on LG/OC during agricultural fire episodes in spring. For a given LG/OC range, F decreased substantially during the day, likely due to photo-blanching of chromophores associated with the ~365 nm peak. The same conclusion could be reached based on K, another indicator for the significance of the ~365 nm peak.